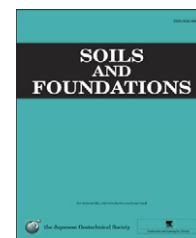




The Japanese Geotechnical Society

Soils and Foundations

www.sciencedirect.com
journal homepage: www.elsevier.com/locate/sandf



Investigation of localized deformation in partially saturated sand under triaxial compression using microfocus X-ray CT with digital image correlation

Yosuke Higo*, Fusao Oka, Tomohiro Sato¹, Yoshiki Matsushima², Sayuri Kimoto

Department of Civil & Earth Resources Engineering, Kyoto University, Japan

Received 21 December 2011; received in revised form 20 August 2012; accepted 14 October 2012

Available online 13 March 2013

Abstract

In this paper, localized deformation in partially saturated sand was investigated quantitatively using microfocus X-ray computed tomography (CT) and an image analysis of the CT images. Triaxial compression tests on a partially saturated dense Toyoura sand specimen were carried out under a low confining pressure and under drained conditions for both air and water. The development of localized deformation was observed macroscopically using microfocus X-ray CT, and the displacement field over the entire specimen was quantified by an image analysis of the CT images with the digital image correlation (DIC) technique. The progressive development of shear bands is discussed with reference to these images. In addition, the region of localization was observed microscopically by partial CT scanning on a micron scale with high spatial resolution. Changes in the particulate structures are also discussed herein. The DIC image analysis of the partial CT images provided a microscopic displacement field and indicated that very fine localized shear deformation developed before the shear bands had become visible in the macroscopic investigation.

© 2013 The Japanese Geotechnical Society. Production and hosting by Elsevier B.V. All rights reserved.

Keywords: Localized deformation; Partially saturated sand; Quantification; Microfocus X-ray CT; Image analysis; International Geotechnical Classification Number: D06

1. Introduction

It is well known that pore water exists between the particles of unsaturated soil, in the form of menisci, due to the surface tension of the water, the hydrophilic nature of the soil particles and the shape of the particles.

The concave side of menisci is air, and the air pressure is larger than the water pressure. The pore water pressure is negative when the air pressure is zero. The negative pressure provides an increase in the inter-particle force, which consequently provides an increase in strength. This is the reason why the strength of unsaturated soil is higher than that of saturated soil. Meanwhile, a breakdown in the suction, e.g., by the infiltration of water and/or shearing, induces a large loss in strength involving clearer shear banding with stronger strain softening than fully saturated or dry sand (e.g., Cui and Delage (1996), Cunningham et al. (2003), Higo et al. (2011a, 2011b)). Strain localization, including shear banding, is one of the most important issues in the field of geomechanics. This is because the phenomenon of strain localization signifies the onset of

*Corresponding author.

E-mail address: higo.yosuke.5z@kyoto-u.ac.jp (Y. Higo).

¹Presently in Maruun Kensetsu, Co. Ltd., Japan.

²Presently in Central Japan Railway Company, Japan.

Peer review under responsibility of The Japanese Geotechnical Society.



failure in geomaterials. From a geotechnical point of view, partially saturated soil structures, including river dikes and road embankments, take advantage of the suction in order to stabilize the soil structures. On the other hand, one of the most significant reasons for the collapse of soil structures is the decrease in suction. Therefore, it is important to clarify the mechanism of the brittle failure of partially saturated soil, which is strongly related to the strain localization phenomenon. A number of experimental investigations has revealed the mechanism of the strain localization phenomenon through the use of some image analysis techniques (e.g., Desrues and Viggiani (2004), Michalowski and Shi (2003), Kodaka et al. (2001)), X-ray radiography (e.g., Roscoe (1970), Vardoulakis and Graf (1982), Muir Wood (2002)) and X-ray computed tomography (e.g., Hicher et al. (1994), Desrues et al. (1996), Otani et al. (2000)). Rudnicki and Rice (1975) explained strain localization theoretically as a bifurcation from homogeneous deformation. Also, numerical analyses based on various kinds of constitutive models have made it possible to successfully simulate strain localization, such as shear bands and/or compaction bands (e.g., Loret and Prévost (1991), Schrefler et al. (1996), Oka et al. (2002), Higo et al. (2006), Oka et al. (2011)). However, the focus of these discussions has mainly been dry and/or fully saturated soil. The strain localization of partially saturated soil is also an important issue because the effect of suction on strain localization is not clear.

The aim of this study is to reveal the strain localization behaviors of partially saturated dense sand under triaxial compression conditions from both a macroscopic and microscopic points of view, for the purpose of clarifying the mechanism of strain localization in partially saturated soil using X-ray computed tomography. It is important to study the deformation behaviors of well-compacted unsaturated sands under low overburden pressures such as river dikes and road embankments since partially saturated soil often exhibits a more brittle mode of failure, especially in the cases of lower confining pressure (e.g. Cui and Delage (1996), Cunningham et al. (2003), Higo et al. (2011a, 2011b)), corresponding to loss in strength due to the collapse of the water meniscus. Thus, the triaxial compression tests were conducted under low confining pressure and drained conditions for air and water using dense sand specimens.

The X-ray CT developed by Hounsfield (1972) in the field of medicine has recently been applied to the field of engineering as a powerful tool for viewing the inside of objects in a nondestructive manner. The X-ray CT technique provides the three-dimensional distributions of the linear attenuation coefficient of objects, which makes it possible to obtain the distribution of density in the objects using the almost linear relation between the attenuation coefficient and the density. Using this relation, Desrues et al. (1996) quantified and discussed the local void ratios inside the shear bands of dry sand. Since then, X-ray CT has been used widely to view the changes in density distribution in geomaterials (e.g., Otani et al. (2000),

Alshibli et al. (2000), Watanabe et al. (2012)). In the last decade, a micro-tomography technique, including micro-focus X-ray CT and micro-CT with synchrotron radiation, has been applied to investigate the microstructures of geomaterials, since the micro-CT images with a micron's level of spatial resolution make it possible to observe sand particles individually (e.g., Oda et al. (2004), Matsushima et al. (2006), Higo et al. (2011a, 2011b)). Moreover, the pore water in partially saturated sand, existing as meniscus, has been successfully viewed through microfocus X-ray CT by the author's research group (Higo et al., 2011a).

Recently, the image analysis of CT images by the digital image correlation (DIC) technique has achieved full-field measurement, i.e., the quantification of the displacement field (e.g., Lenoir et al. (2007), Viggiani et al. (2010), Hall et al. (2010)). In the DIC analysis, the translation of the points arbitrarily specified in the reference image to the deformed image is determined by optimizing the cross-correlation coefficient calculated in the correlation window employed around the reference point. An image analysis using digital camera images, such as two-dimensional DIC and PIV, provides a two-dimensional surface displacement field, while DIC with CT images, referred to as *volumetric* digital image correlation, provides a three-dimensional displacement field. In addition, the displacement field obtained by DIC can provide the three-dimensional distributions of shear strain and volumetric strain by employing spatial gradients of some interpolation functions, although CT images themselves, without DIC, yield only the changes in density.

In the present study, the strain localization of partially saturated sand during triaxial compression tests has been discussed through the visualization of the changes in density in the specimen using microfocus X-ray CT and the quantification of the displacement field in the specimen by a DIC image analysis. In addition to the foregoing macroscopic investigation, i.e., observations of the entire specimen, particulate structural changes in the particular volume, including shear bands, has been discussed from a microscopic point of view using the partial CT images. The purpose of the partial CT scan is to view only the volume of interest, not the entire specimen, with a much higher spatial resolution, namely, enough to distinguish the air, the water and the solid phases from each other. A trinarization technique is proposed in this paper, by which the three phases are successfully quantified. Furthermore, the DIC of the partial CT images provides the very thin localized shear deformation developing before the shear bands become visible in the macroscopic observations.

2. Materials and methods

2.1. Test sample and specimen preparation

The test sample used in this study is a type of silica sand called Toyoura sand. The physical properties include a particle density of 2.64 g/cm³, a maximum void ratio of 0.975, a minimum void ratio of 0.614 and a fines content of 0.1%. Toyoura sand used is uniform (the uniformity coefficient is

1.6) and semi-angular in shape with an average diameter D_{50} of 0.185 mm.

The specimen was prepared by the moist-tamping method. The dry sand mixed with deaired water was compacted in a mold to be a dense specimen with an initial void ratio of 0.665 and a relative density D_r of 85.9%. The water content was 15.2% and the degree of saturation of the specimen was 60.4%. The degree of saturation was selected to be almost the same as that in previous experimental results (Higo et al., 2011a, 2011b). The suction corresponding to the degree of saturation (58.62%) effectively increases the strength of the partially saturated Toyoura sand so that it is stronger than fully saturated and air-dried sands. The specimen was 70 mm in height and 35 mm in diameter. The five layers each had a thickness of 14 mm. After the compaction of each layer, the top surface of the layer was disturbed in order to make the connectivity between the layers homogeneous.

Toyouura sand usually includes iron sand particles, as shown in Fig. 1. It is seen in the CT image that the iron sand particles correspond to the lighter portions since they have a higher attenuation coefficient than Toyoura sand particles. This made it possible to use the iron particles in the sand as markers in the specimen. The iron sand was collected by use of a magnetic field and put between the compaction layers, as shown in Fig. 2. These two marker layers were installed 2.8 and 1.4 cm below the top of the specimen. A total of 0.5 g of iron sand was in each layer.

2.2. Testing procedure for triaxial tests with X-ray computed tomography

The specimen was placed in a thin lucid acrylic cell, which is almost completely transparent when subjected to X-rays. A confining pressure of 50 kPa was applied by air pressure without any back pressure. The top and the bottom of the specimen were exposed to the atmosphere. The air pressure was equal to the atmospheric pressure and the amount of pore water was constant. It should be noted that no drained water was measured during the triaxial tests. The top and the bottom boundaries were not

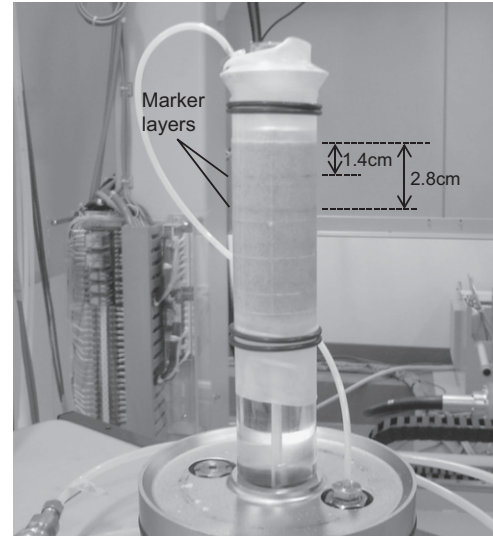


Fig. 2. Location of the marker layers.

lubricated in the present experiment. The axial load was applied through a displacement control system with a constant axial strain rate of 0.5%/min until an axial strain of 20%.

The microfocus X-ray CT apparatus used in the present study is the KYOTO-GEO μ XCT (TOSCANER-32250 μ HDK) installed in the Department of Civil & Earth Resources Engineering of Kyoto University (Higo et al., 2010, 2011a). A schema of the microfocus X-ray CT apparatus is illustrated in Fig. 3. The minimum spot size of the X-ray source is 4 μ m, which achieves a spatial resolution of 5 μ m. Users can control the voltage (maximum of 225 kV) and the current (maximum of 1 mA) of the X-ray source individually up to a maximum energy of 200 W. In addition, it is possible to manually control the magnification by changing the location of the rotation table on which the specimen is placed and the X-ray image intensifier (detector). The magnification can also be controlled by selecting different sizes of detectors.

The reconstruction of the attenuation records of the X-ray provides CT images, i.e., the distribution of the CT values, which linearly relate to linear attenuation coefficient μ defined as follows:

$$I = I_0 \exp(\mu x) \tag{1}$$

where I_0 is the incident X-ray intensity, I is the attenuated X-ray intensity and x is the path length through the object. It is well known that the relation between the CT value and the density of the objects are linear. In addition, the same CT values can be obtained in principle through the use of the same scanning conditions, such as the X-ray tube voltage and current, the distance between the X-ray source and the rotation table, the distance between the X-ray source and the detector and the size of the detector. Thus, the relative changes in density can be discussed through the changes in the CT values obtained under the same scanning conditions. Note that the CT values are linearly

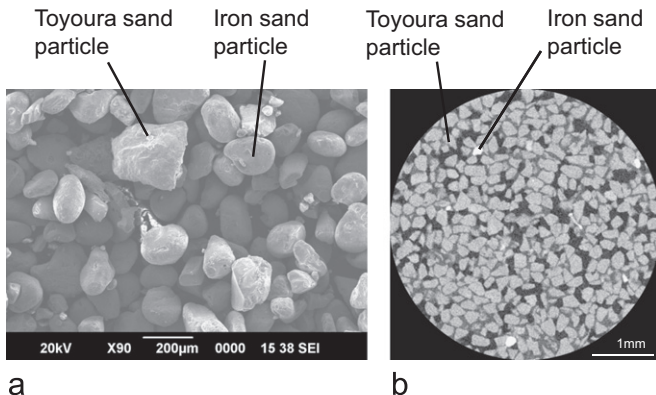


Fig. 1. SEM image and CT image of Toyoura sand and iron sand particles.

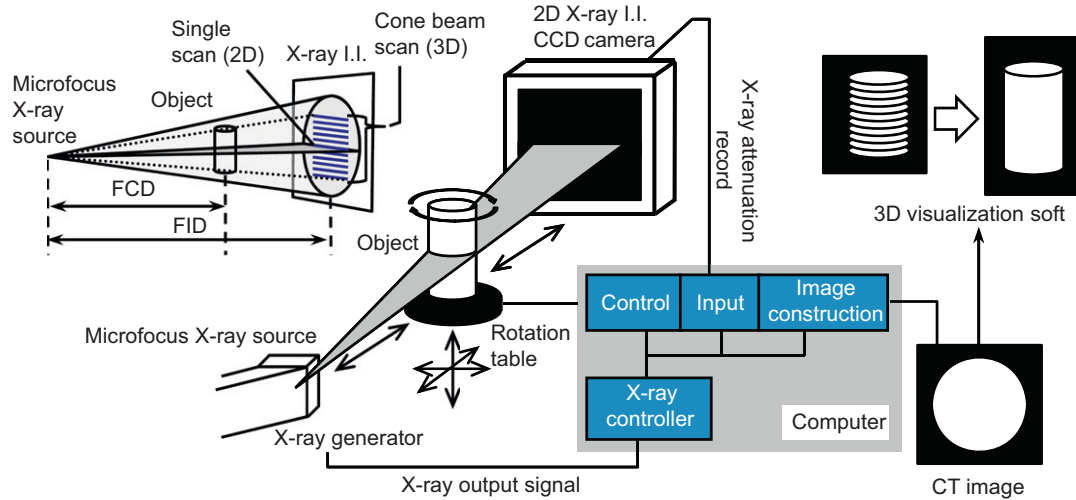


Fig. 3. Schematic illustration of the microfocus X-ray CT system used in this study.

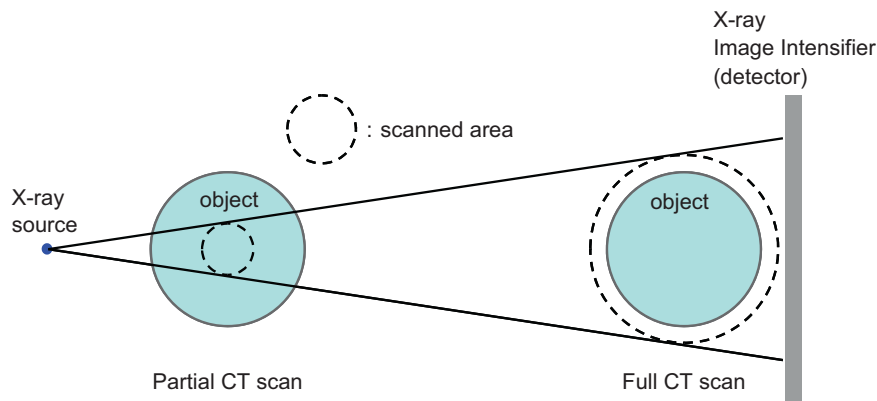


Fig. 4. Schematic figure of comparison between the full CT and the partial CT.

transformed into gray values of 14 bits; they are then converted into jpeg images of 8 bits in the CT images shown in the present paper.

Two types of X-ray CT scanning were performed at axial strains of 0% (initial state), 2%, 4%, 8%, 15% and 20%. One type is the full CT scan, by which the entire specimen is scanned, and the other type is the partial CT scan, which provides CT images of the partial volume of interest with higher magnification (see Fig. 4). The partial CT scan was taken just above the upper marker layer, because we have discovered through pre-performed tests that shear bands often appear in that region. It took about two hours to complete both the full CT scan and the partial CT scan. The axial loading was stopped during the scans to avoid the movement of the specimen due to loading. After scanning, the axial loading was started again at the same axial strain rate.

2.3. Digital image correlation

The digital image correlation (DIC) technique was originally proposed by a research group at the University

of South Carolina (e.g., Peters and Ranson (1981), Chu et al. (1985)) to obtain the full-field surface displacements in materials under deformation by comparing the digital images of the specimen surface in the reference and the deformed states. Since then, the DIC method has been extensively improved and widely used in experimental mechanics as a powerful and flexible tool for deformation measurement. Recently, DIC has been applied to quantify three-dimensional displacements using X-ray CT images as a direct extension of the two-dimensional DIC method (e.g., Bay et al. (1999)). In the field of geomechanics, a research group at the University of Grenoble has applied the three-dimensional DIC to visualize the strain localization in both soft rock and sand during triaxial compression using CT images (Lenoir et al., 2007; Viggiani et al., 2010; Hall et al., 2010), in which internal full-field deformations are provided by tracking the movement of the volume unit (subset); the method is referred to as volumetric DIC.

The procedure of the DIC method used in this study is similar to that of Lenoir et al. (2007). A schematic illustration of the procedure is shown in Fig. 5. At first, the CT images of the reference and the deformed states are

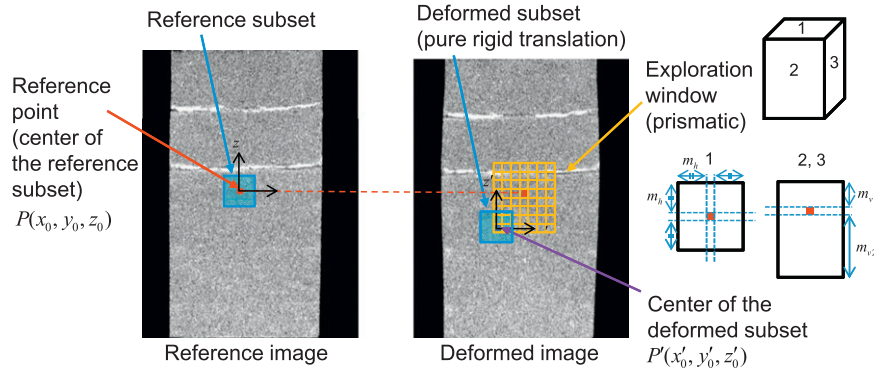


Fig. 5. Explanation of the procedure and the parameters of digital image correlation analysis.

prepared. Each voxel (minimum unit volume) has a gray level of 14 bits and the assembly of the voxels forms the whole CT images. The locations of the reference points (voxels, in practice), $P(x, y, z)$, at which the displacements are calculated, are determined in the reference image. In the present study, the reference points are placed in a grid pattern, since it is convenient to use a shape function of the eight-node isoparametric finite element to calculate strain.

The next step is to search for the corresponding points in the deformed image. A reference subset, referred to as the “correlation window” of the $(2n + 1) \times (2n + 1) \times (2n + 1)$ voxels, centered at reference point $P(x_0, y_0, z_0)$ from the reference image, is chosen and used to track its corresponding location in the deformed image. x_i, y_i and z_i are the coordinates in the reference subset. The degree of similarity between the reference subset and the deformed subset is evaluated by a cross-correlation criterion or the sum of the squared difference criterion. In the present study, a zero-normalized cross-correlation coefficient, R , which offers the most robust noise-proof performance (Pan et al., 2009), is used, namely,

$$R = \frac{\sum_{i=-n}^n \sum_{j=-n}^n \sum_{k=-n}^n [f(x_i, y_j, z_k) - f_m] \times [g(x'_i, y'_j, z'_k) - g_m]}{\Delta f \Delta g} \quad (2)$$

in which

$$f_m = \frac{1}{(2n + 1)^3} \sum_{i=-n}^n \sum_{j=-n}^n \sum_{k=-n}^n f(x_i, y_j, z_k)$$

$$g_m = \frac{1}{(2n + 1)^3} \sum_{i=-n}^n \sum_{j=-n}^n \sum_{k=-n}^n g(x'_i, y'_j, z'_k)$$

$$\Delta f = \sqrt{\sum_{i=-n}^n \sum_{j=-n}^n \sum_{k=-n}^n [f(x_i, y_j, z_k) - f_m]^2}$$

$$\Delta g = \sqrt{\sum_{i=-n}^n \sum_{j=-n}^n \sum_{k=-n}^n [g(x'_i, y'_j, z'_k) - g_m]^2}$$

where x'_i, y'_i and z'_i are the coordinates in the deformed subset, the center point is $P'(x'_0, y'_0, z'_0)$, and $f(x)$ and $g(x)$ are intensity values, the gray values in this study, at the point x in the reference image and the deformed image, respectively.

Corresponding to global deformation, it can be assumed that the shape of the reference subset is changed in the deformed image. The deformation of the subset can be given by shape functions ξ, η and ζ for the three directions, i.e.,

$$\begin{aligned} x'_i &= x_i + \xi(x_i, y_i, z_i) \\ y'_i &= y_i + \eta(x_i, y_i, z_i) \\ z'_i &= z_i + \zeta(x_i, y_i, z_i) \end{aligned} \quad (3)$$

In the present study, a zero-order shape function is used, namely, a pure rigid translation is assumed. This is because the deformations between the two images employed in this study are small enough to disregard the deformation of the subset. Higher order shape functions should be used when changes in shape and the rotation of the deformed subset are significant (Hubert and Sutton, 2002).

Once the peak position of correlation coefficient R has been detected in the deformed image, the displacement vector is given by the difference in the positions of the reference subset center, $P(x_0, y_0, z_0)$, and the deformed subset center, $P'(x'_0, y'_0, z'_0)$. The peak position for correlation coefficient R is searched for only in the “exploration window” in order to reduce the computational time. The exploration window is prismatic in shape, as illustrated in Fig. 5, and is chosen where the translation point can be deduced from the global deformation of the specimen. In Fig. 5, m_h, m_{v1} and m_{v2} are parameters denoting the size of the exploration window. m_{v1} can be smaller than m_{v2} when the specimen is compressed from the top end because all the points in the specimen probably move downward corresponding to the global deformation of the specimen.

3. Results and discussions

3.1. Macroscopic investigation of localized deformation

Fig. 6 shows the stress–strain relation and the volumetric strain–axial strain relation in which the compression is

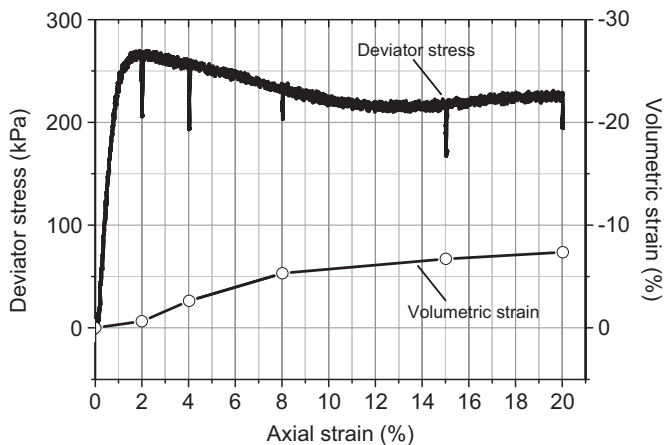


Fig. 6. Stress–strain relation and the relation between the volumetric strain and the axial strain (compression is positive).

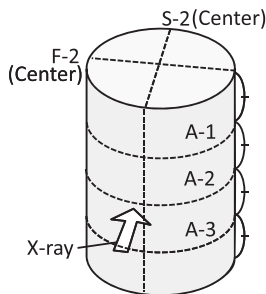


Fig. 7. Locations of the cross sections for the full CT images.

positive. It is seen that the stress relaxation occurs at each step of X-ray scanning because the axial loading was paused and the axial strain was fixed during the scanning process. It took about two hours for both the full CT scanning and the partial CT scanning. The deviator stress increased until it reached the same stress level as just before the X-ray scanning at the same strain rate. The volumetric strain was calculated by the integration of the voxels occupying the specimen through which the volume of the specimen was accurately measured even for the partially saturated soil (see Higo et al. (2011a)). The peak deviator stress was observed at an axial strain of 2%, after which strain softening occurs. At large axial strain levels of more than 13%, the deviator stress increases slightly, but was almost constant, i.e., it was at the residual stress level, and the increment of volumetric strain was much smaller than that at the smaller axial strain levels. This indicates that the specimen almost reaches the critical state. The volumetric strain–axial strain relationships indicate that the specimen exhibits expansive volumetric strain. It is seen that the increasing rate of the volumetric strain becomes large when strain softening starts and becomes moderate in the residual state. The increase in volumetric strain corresponding to the variation in deviator stress suggests the development of positive dilatancy, i.e., volume expansion due to shearing.

The locations of the cross sections for the full CT images are indicated in Fig. 7. The cross sections are chosen to demonstrate the deformation mode of the specimen representatively. S-2 and F-2 vertical cross sections include the center of the specimen and are parallel and perpendicular to the direction of X-ray, respectively.

Fig. 8 shows the full CT images taken during the triaxial compression, and the scanning conditions are listed in Table 1. The two white lines in the vertical cross sections and the white regions in the horizontal cross section of A-1 at an axial strain of 20% indicate the marker layers of the iron sand. The CT image is uniformly light gray at the initial state, which indicates that the moist-tamping method used to ensure the homogeneity of the specimen in the preparation stage was successful. At an axial strain of 2%, corresponding to the peak stress, the distribution of CT values indicates the specimen is homogeneous. Just after the peak stress, at an axial strain of 4%, it can be seen that the specimen starts to deform to a barrel-like shape and that the center part of the specimen becomes slightly darker, i.e., the density becomes lower than that of the initial state. The lower density regions expand and are localized at an axial strain of 8%, while the localization of the lower density regions becomes clearer and asymmetric at an axial strain of 15%. Finally, a clear localization zone is seen to develop in the specimen. We can see in the horizontal images, at axial strain levels of 15% and 20%, both radial and circular localization. In the vertical images, V-shaped and inverted V-shaped localizations are observed in the upper and the lower sections, respectively. That is, cone type localization appears in both the upper part and the bottom part, around which the radial localizations are formed. This type of localization mode is similar to that observed in the triaxial specimens of dry sands by Desrues et al. (1996), Alshibli et al. (2000), Batiste et al. (2004), and also in fully saturated sands by Higo et al. (2011a, 2011b). We have, therefore, found that the strain localization mode of partially saturated sand finally develops in the critical state, which is similar to the air-dried and the fully saturated sands. It should be noted that this localization clearly develops in the case of partially saturated sand (Higo et al., 2011a, 2011b).

It seems that the localization of the lower density regions indicates shear bands, which correspond to positive dilatancy associated with shear deformation. This tendency is consistent with the volume expansion that occurs with the deviator stress seen in the stress–strain relation and the volumetric strain–axial strain relation (Fig. 6). In addition, the inclination of the marker layers discontinuously changes at the point crossing the lower density regions, as can be seen in Fig. 9. This deformation mode seems to be associated with shear deformation. However, it is necessary to quantify “shear deformation” in order to confirm that shear bands are developing in the specimen, because CT images only provide the changes in density explicitly.

In Table 2, parameters for DIC are listed. The reference points were placed evenly at an interval of 40 voxels in

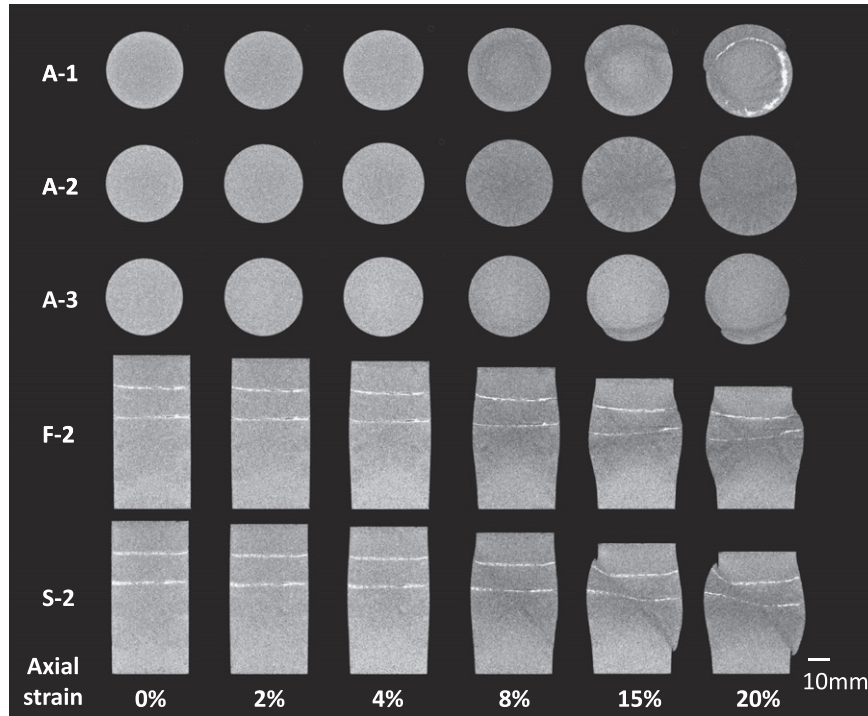


Fig. 8. Full CT images.

Table 1
X-ray CT scanning conditions.

	Full CT [‡]	Partial CT	Partial CT without triaxial cell
Voltage (kV)	130	130	130
Current (μA)	200	300	200
Size of X-ray I.I. (inch)	9	6	6
Projection views	1200	4800	4800
Accumulation	10	20	20
Image size	1024 × 1024	1024 × 1024	1024 × 1024
Number of images	600	280	140
Voxel size ^a (μm)	75.7 ² × 118.0	7.6 ² × 12.0	4.2 ² × 7.0

[‡] Aluminum filter with thickness of 1 mm is installed just in front of the X-ray source in the case of full CT.

^aVoxel size: (pixel size)² × (thickness) of one CT image.

horizontal and vertical directions, while those outside the specimen were omitted from the analysis. Note that the length between two reference points in the vertical direction is longer than that in the horizontal direction since the thickness of a voxel is longer than the length of the other two sides.

The distribution of incremental displacement vectors obtained by the DIC analysis is shown in Fig. 10. It is seen that the displacements at the upper part of the specimen are larger than those at the lower part since the axial loading was applied by the compelled vertical displacement from the top. In Fig. 10(b), the displacement continuously decreases from the top to the bottom before the axial strain reaches

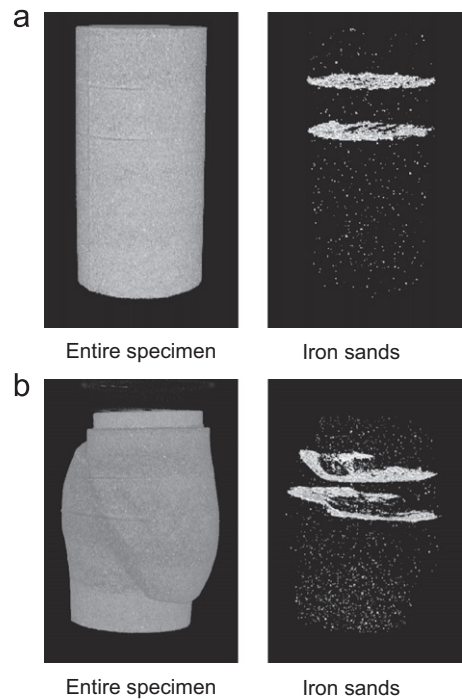


Fig. 9. Deformations of marker layers at the initial state and an axial strain of (a) 0% and (b) 20%.

4%, while it becomes relatively discontinuous at an axial strain of 8% in Fig. 10(c). In Fig. 10(d) and (e), the boundary between the larger and the smaller displacement region can be observed and progressively inclined where the

Table 2
Parameters for the three-dimensional DIC analysis.

Process	A	B	C	D	E
Axial strain before deformation (%)	0	2	4	8	15
Axial strain after deformation (%)	2	4	8	15	20
Size of the analysis domain (voxel)	600 × 600 × 600				
Voxel size ^a (μm)	75.7 ² × 118.0				
Interval of the reference points (voxel)	40				
Size of the exploration window m_h, m_{v1}, m_{v2} (voxel)	20, 10, 30	20, 10, 30	20, 10, 30	20, 10, 40	20, 10, 30
Size of the correlation window n (voxel)	10				

^aVoxel size: (pixel size)² × (thickness) of one CT image.

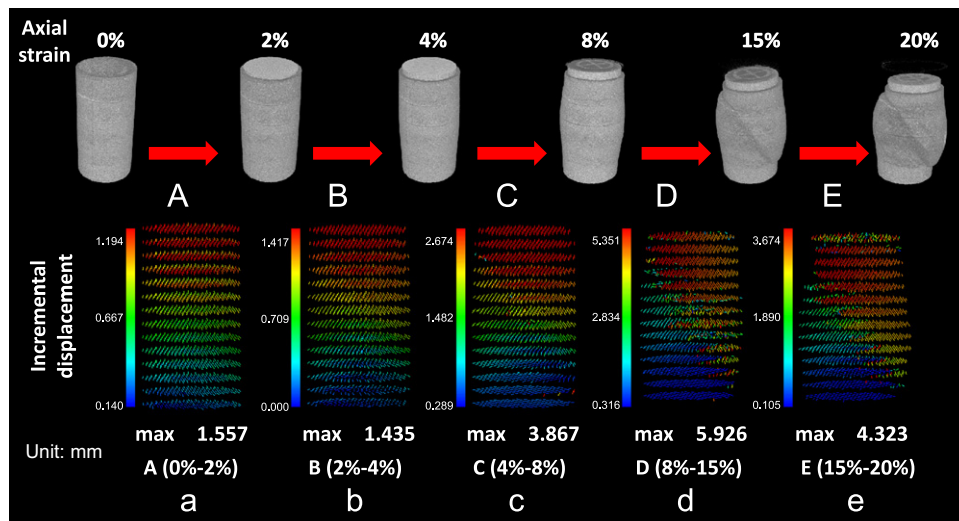


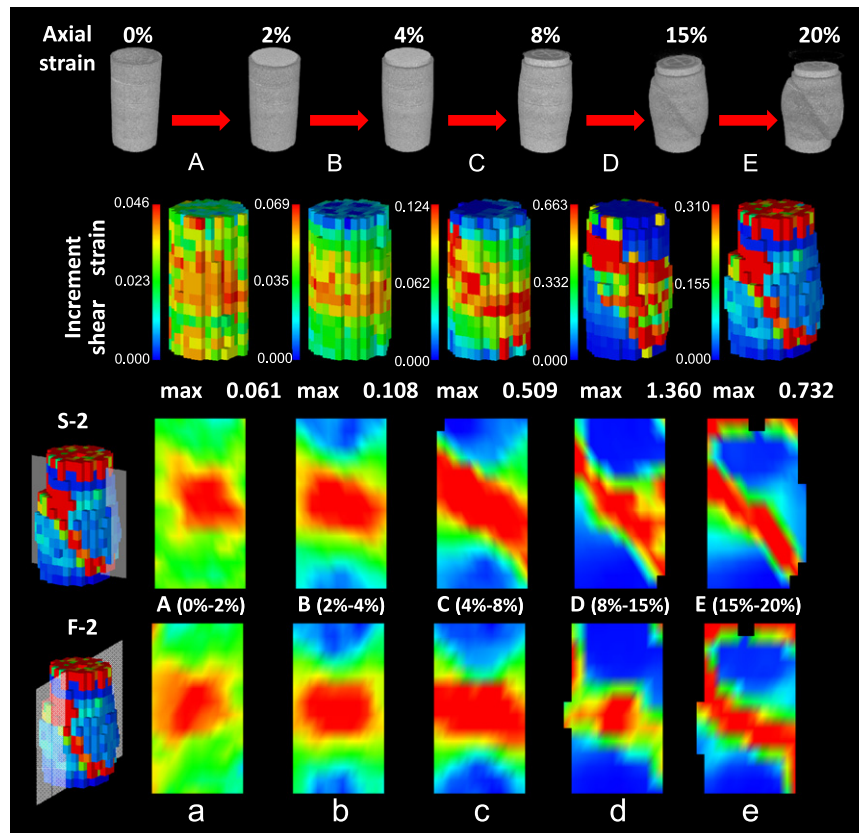
Fig. 10. Distributions of the incremental displacement obtained by the DIC analysis.

displacements above the boundary are much larger than those below the boundary.

Figs. 11 and 12 shows the distributions of incremental shear strain and volumetric strain, respectively. The strain levels were provided by adopting the B matrix for the eight-node isoparametric finite elements. The incremental volumetric strain is defined as a trace of strain increment tensor $d\epsilon_{ij}$ ($i, j = 1, 2, 3$), and the second invariant of incremental deviatoric strain tensor de_{ij} ($= d\epsilon_{ij} - d\epsilon_{kk}\delta_{ij}$, $i, j = 1, 2, 3$) is herein referred to as the shear strain increment. It can be clearly seen that the shear strain and the expansive volumetric strain localize with an increase in the axial strain, and that the localized areas of shear strain correspond to the lower density regions observed in the CT images in Fig. 8 and the location of the discontinuous boundary in the displacement field in Fig. 10. According to the mathematical definition of shear bands (e.g., Vardoulakis and Sulem (1995)), namely, “a thin layer that is bounded by two parallel material discontinuity surfaces of the incremental displacement gradient”, it can be concluded that shear band with positive dilatancy develops in the specimen. In addition, the DIC results indicate that shear strain localizes even at an axial strain of 2% and that the

X-shaped strain localization becomes clearly visible at an axial strain of 4%. Furthermore, the distributions of shear strain at axial strain levels of 2% and 4% are slightly asymmetric. Namely, the preferable inclination of the development of the shear band already appears at an axial strain of the peak deviator stress level, whereas the localized deformation in the CT images is not visible at axial strain levels of 2% and 4% and the localization still seems to be symmetric even at an axial strain of 8%.

The volume compression occurs at the top and the bottom of the specimen probably because of the friction caused by the top cap and the bottom pedestal, while the volume expansion is observed in the middle part of the specimen. In the region with large axial strain where the significant shear band becomes visible in the CT images, in Fig. 12(d) and (e), it is interesting that the compressive strain also localizes along with the shear band, although the specimen exhibits expansion globally. Similar strain distributions have been found for dry sands by Watanabe et al. (2010) and Hall et al. (2010). Further study is required on this point through precise investigation of the microstructural changes along the shear band.



At the top of the specimen, DIC results with the low correlation coefficients have been omitted.

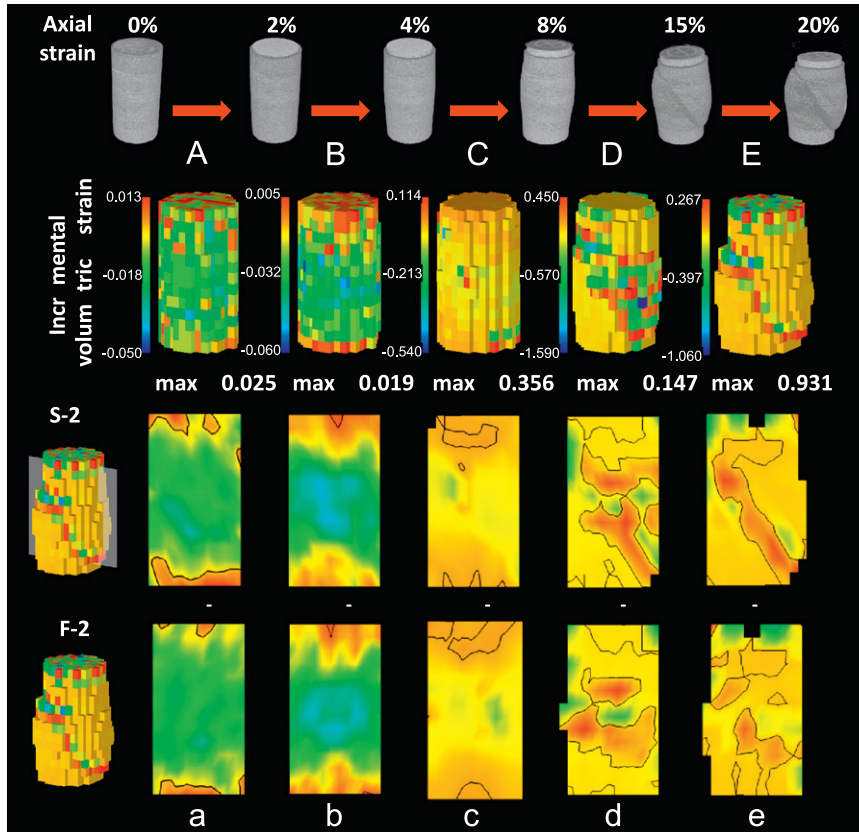
Fig. 11. Distribution of the incremental shear strain obtained by the DIC analysis.

3.2. Microscopic investigation of localized deformation

Partial CT images are shown in Fig. 13, in which the location of the partial CT is indicated in the vertical cross section of the full CT image. These partial CT images were taken under the confining pressure, just after the full CT scan for each axial strain level without any unloading. The voxel size of the partial CT scan is $7.6^2 \times 12.0 \mu\text{m}$ (see Table 1). The scan area is a small cylinder with a height of 3.36 mm and a diameter of 7.78 mm. The scan area of each step is determined to make the center of the scan area about 4.5 mm above the upper marker layer and the left side about 2 mm away from the left boundary of the S-2 cross section. It is seen in the partial CT images of S-2L and A-2L that the left area is darker than the right area. This is an artifact when the scan area of the partial CT scan is distant from the center of the specimen because of the difference in the length of the X-ray passing through the object among the points in the specimen, whereas the path length through object x in Eq. (1), used during the reconstruction of the CT images, is constant for all of the points. In particular, the path lengths of the points close to the outside of the specimen are shorter than those close to the center of the specimen, which makes the points close to the outside darker than those close to the inside. It should

be noted that this artifact is different from the beam-hardening artifact which makes the center part of the object darker than the outside.

In the partial CT images of S-2L and A-2L of Fig. 13, we can see that the sand particles and the voids are clearly distinguished and that the voids are composed of pore water and pore air indicated by dark gray and black, respectively. At the initial state, before the triaxial cell was installed, a partial CT scan of the specimen was additionally performed with a finer spatial resolution. During this scanning, vacuum of 20 kPa was applied to the inside of the specimen as the confining pressure to stabilize the specimen. One reason for not using the cell was that the magnification is larger when the specimen is much closer to the X-ray source. The other reason was to avoid the X-ray attenuation which occurs due to the cell, which degrades the spatial resolution of the CT images. Fig. 14(a) shows the partial CT image without the triaxial cell. The voxel size is $4.2^2 \times 7.0 \mu\text{m}$ (see Table 1) and the height and the diameter of the scan area are 0.98 and 4.34 mm, respectively. The location of this scan is the center of the specimen, i.e., the center of the scan area is on the center line of the specimen and 35 mm below the top of the specimen, which makes it possible to avoid the artifact of the partial CT scanning, as previously mentioned. In these



At the top of the specimen, DIC results with the low correlation coefficients have been omitted.

Fig. 12. Distribution of the incremental volumetric strain obtained by the DIC analysis (compression is positive, black lines are contour lines of zero-volumetric strain).

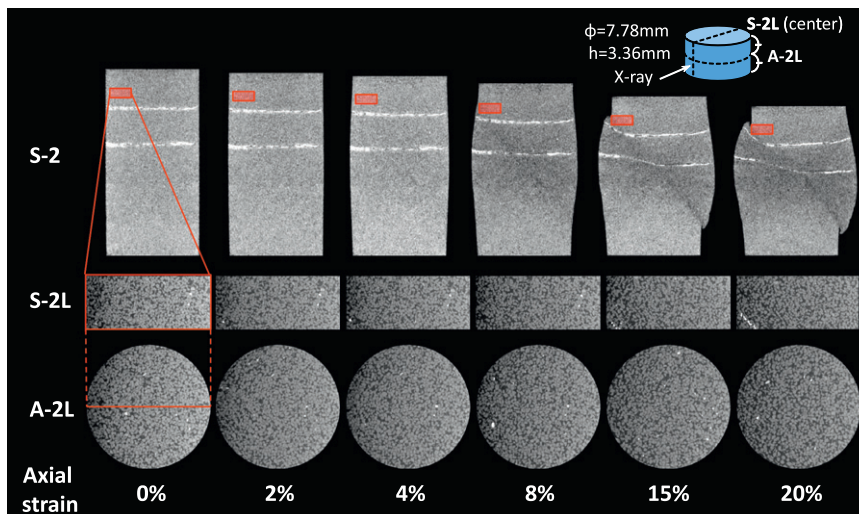


Fig. 13. Partial CT images under confining pressure and the vertical cross sections of the full CT images with the location of the partial CT scanning.

CT images, the shape of the soil particle and the pore water can be observed more clearly. Furthermore, we have tried to identify the solid phase, the water phase and the air phase individually by a trinarization technique with the region growing method shown in Appendix. The trinarized

images are shown in Fig. 14(b), where the blue portions indicate the pore water, and the black and the light brown portions indicate pore air and soil particles, respectively. It can be seen that pore water exists in the smaller voids where several particles contact or gather closely to each

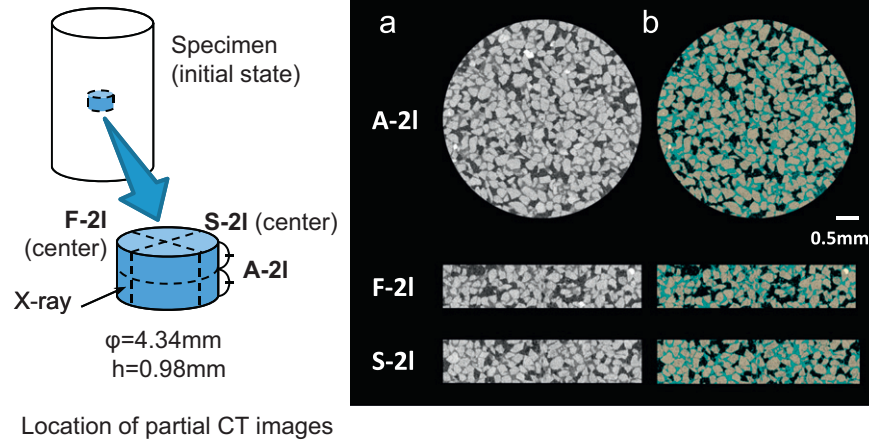


Fig. 14. Partial CT images without the triaxial cell at the initial state: (a) original image; (b) trinarized image (blue: pore water, black: pore air, light brown: soil particles). (For interpretation of the references to color in this figure legend, the reader is referred to the web version of this article.)

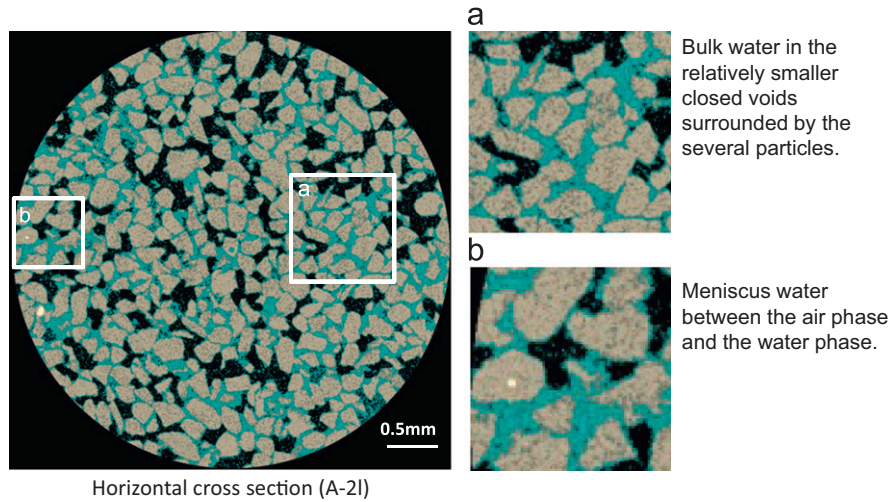


Fig. 15. Meniscus water and the bulk water at the initial state.

other, while the pore air is mostly in the larger voids. The two areas are highlighted in Fig. 15. The meniscus can be clearly seen between the air phase and the water phase. Meanwhile, the bulk water can be seen in the relatively smaller closed voids surrounded by the several particles.

Assuming the identical spherical sand grain and an air-water interface described by resembling a typical saddle-shaped meniscus water, we have roughly traced the meniscus and the sand particle as shown in Fig. 16. Two menisci have been assumed between the grains 1 and 2 and between grains 1 and 3. When the air pressure can be assumed to be the atmospheric pressure, the matric suction p_c can be given by the following simple mathematical expression (e.g., Lu and Likos (2004)), namely,

$$p_c = T_s \left(\frac{1}{r_i} - \frac{1}{R_i} \right) \quad (4)$$

where r_i and R_i are the radii of the meniscus shown in Fig. 16 and T_s is the surface tension of the water. Using $T_s = 72.75 \text{ mN/m}$ when the temperature is 20°C and the

radii r_i and R_i measured in the image, the matric suctions can be calculated as follows:

$$p_{c1} = 72.75(\text{mN/m}) \left(\frac{1}{0.0243 \times 10^{-3}(\text{m})} - \frac{1}{0.0542 \times 10^{-3}(\text{m})} \right) = 1.65(\text{kN/m}^2)$$

$$p_{c2} = 72.75(\text{mN/m}) \left(\frac{1}{0.0209 \times 10^{-3}(\text{m})} - \frac{1}{0.0553 \times 10^{-3}(\text{m})} \right) = 2.17(\text{kN/m}^2)$$

Hence, the matric suction among these particles is about 2 kPa. This is comparable to the suction level of the water-retention curve at a degree of saturation of 60.4% for the dense Toyoura sand obtained by the authors' group (Morishita et al., 2012), in which the relative density of the specimen is 74.5%. Namely, the local suction at this point is similar to the average suction of the whole specimen.

Fig. 17 shows the changes in the particulate structure from the initial state to an axial strain of 8%. The particles can be seen to move, which changes the microstructure. Placing focus on the region highlighted by the circle, the black portions grow wider with an increase in axial strain.

This means that the voids are getting larger and the volume expansion, due to positive dilatancy, occurs during the triaxial shearing. Rotation of each grain is seen to be small at these axial strain levels.

In order to evaluate these kinds of microstructural changes quantitatively, the DIC technique has been applied to the partial CT images. From a microscopic point of view, it is important to use sufficiently fine reference points for discussion. In this analysis, we have applied the two-dimensional DIC to the vertical slice, the cross sections S-2L in Fig. 13. In the present analysis, axisymmetric conditions can be assumed before the axial strain reaches 8%,

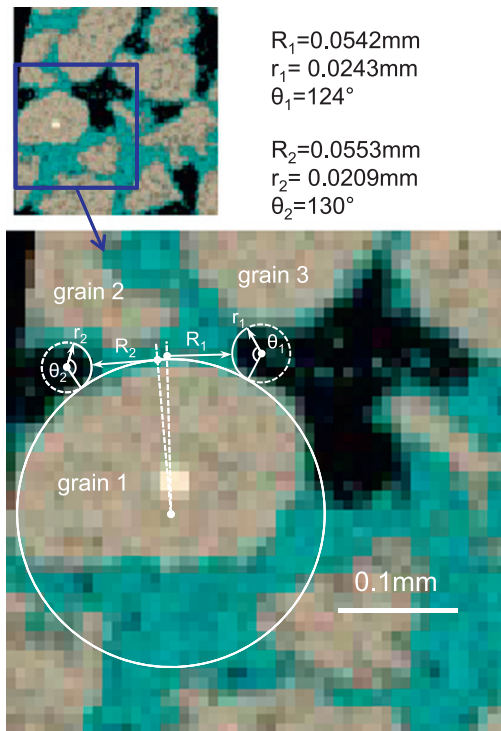


Fig. 16. Menisci and the sand grain described assuming the typical saddle shape and identical spherical particle.

since the asymmetry of the deformation mode is still not significant at this moment. The two-dimensional DIC analysis conditions are listed in Table 3.

Distributions of displacement vectors are shown in Fig. 18(i), in which the displacement vectors with the low correlation coefficients have been omitted. The artifact by the partial CT scan which degrades the resolution of the area close to the outside of the specimen may influence the quality of correlation. It should be noted that the displacements are shifted corresponding to the location of the scanning area in order to trace the specific particles on which focus is placed and by which the changes in particulate structures were observed.

It is seen in Fig. 18(i)(a) that the right part, closer to the center of the specimen, is displaced in a vertically downward direction, while the center and the left parts, closer to the outside of the specimen, are displaced in an upward and horizontal (to the left) direction. The transition of the displacement vector from the right to the left is rather continuous at this moment. The same tendency can be seen in Fig. 18(i)(b). While in Fig. 18(i)(c) the transition region moves to the left, compared with the former two cases, and that the transition region comes to have a band-like shape whose width is relatively narrow. This seems to be a bifurcation phenomenon from a continuous deformation to a discontinuous one. This kind of sharp discontinuity is not visible in either the full CT images or the DIC results for the entire specimen at axial strain levels of 4% and 8%.

In Fig. 18(ii) and (iii), the distributions of the shear strain increments and the volumetric strain increments are shown, respectively. Note that these strain increments are calculated under two-dimensional conditions, namely, incremental volumetric strain $d\epsilon_{kk}$ ($k=1,2$) and the second invariant of incremental deviatoric strain tensor de_{ij} ($=d\epsilon_{ij}-d\epsilon_{kk}\delta_{ij}$, $i,j=1,2$). It can be seen in Fig. 18(ii)(c) and Fig. 19 that the shear strain localizes in the same area of discontinuity of the displacement field. As for the distribution of the volumetric strain, clear strain localization cannot be observed.

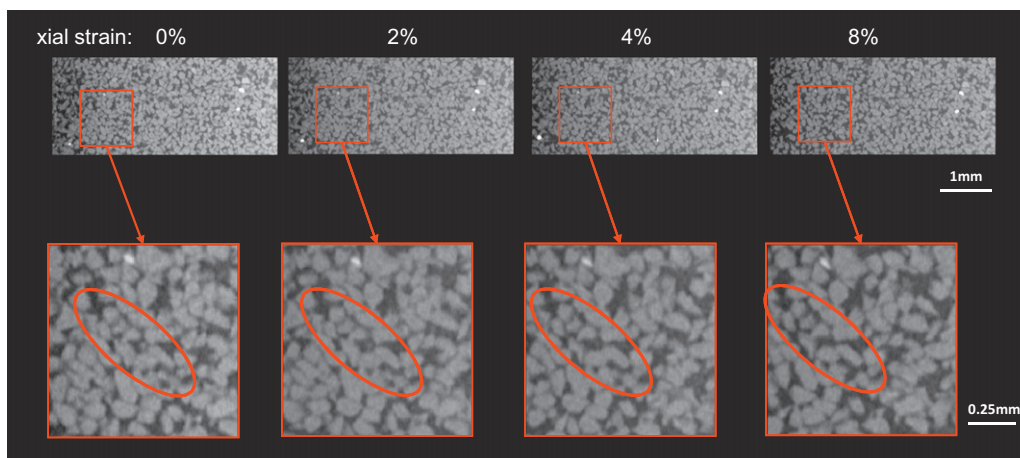
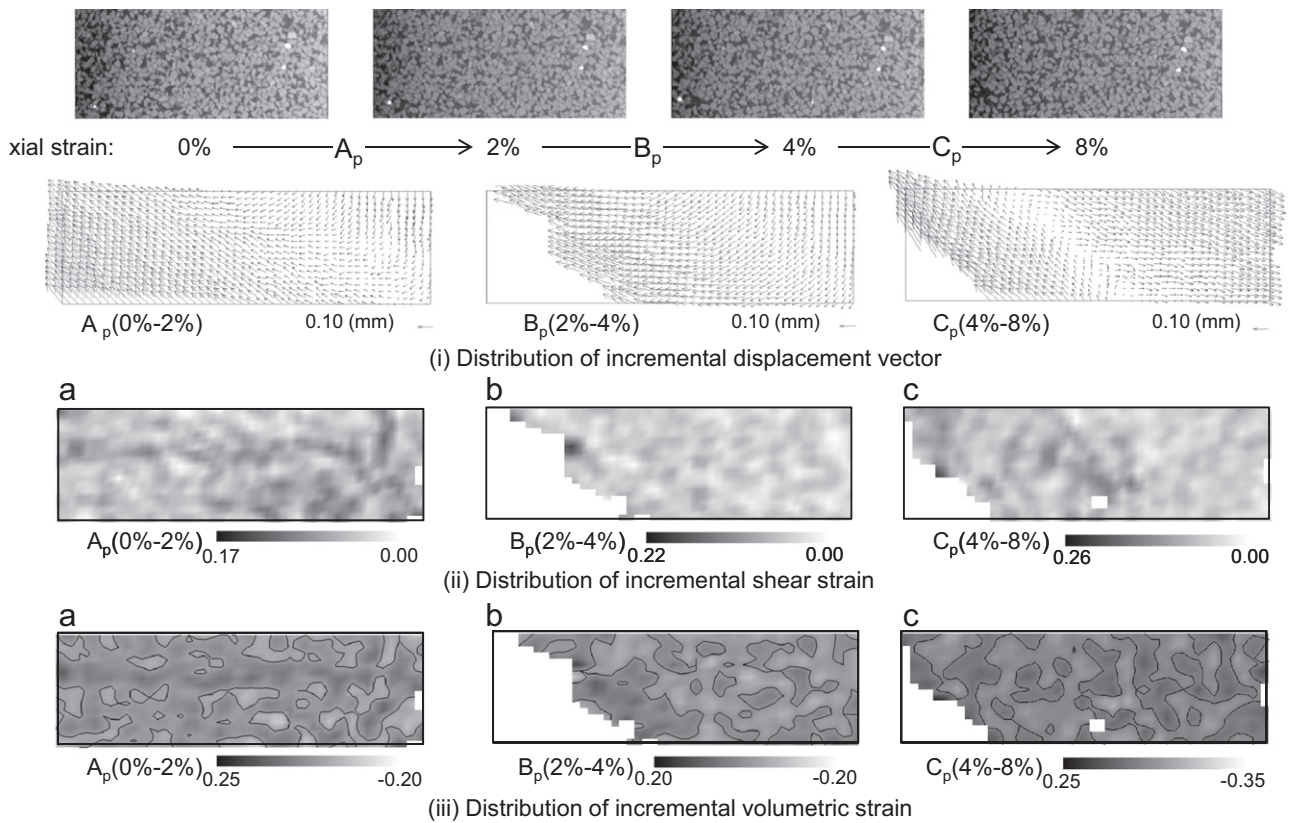


Fig. 17. Microstructural changes observed in the partial CT images (from the initial state to the axial strain of 8%).

Table 3
Parameters for the two-dimensional DIC analysis.

Process	A_p	B_p	C_p
Axial strain before deformation (%)	0	2	4
Axial strain after deformation (%)	2	4	8
Size of the analysis domain (pixel)	240 × 1024		
Pixel size (μm)	12.0 × 7.5		
Interval of the reference points (voxel)	Vertical direction: 10 Horizontal direction: 20		
Size of the exploration window m_i (pixel)	15	15	15
Size of the correlation window n (voxel)	15		

† Pixel size: (vertical side)×(horizontal side).



DIC results with the low correlation coefficients have been omitted indicated by white regions

Fig. 18. Two-dimensional DIC analysis of vertical cross section S-2L of the partial CT images: distributions of (a) the incremental displacement vector; (b) the incremental shear strain; (c) the incremental volumetric strain (compression is positive, black lines are contour lines of zero-volumetric strain).

The localized deformation viewed in the DIC results of the partial CT images can be regarded as shear offset rather than a shear band. A “shear band” usually has a certain thickness involving positive/negative dilatancy, while “shear offset” indicates a gap caused by thin localized shear deformation (e.g., Mollema and Antonellini (1996)). The width of the discontinuity of the displacement, measured in the figure, is 0.84 mm, roughly five times D_{50} , which is much smaller than the width of the shear band globally developed in the specimen, e.g., 1.75 and 2.49 mm (Fig. 19). In addition, the width of the shear band reported

for the unsaturated Toyoura sand (Higo et al., 2011a) and that for the dry Toyoura sand (Oda et al., 2004) are about 10 times the D_{50} . The inclination angle of the narrow localization zone is 45°, while the angles of the global shear bands include 48° and 51°. The narrow localized shear deformation occurs in the specimen before the significant shear band develops globally in the specimen. It seems that this kind of narrow localized shear deformation is one of the reasons for the macroscopic strain softening. Furthermore, it is possible that the breakage of bonding, associated with the disappearance of the meniscus water, leads

to the narrow localized shear deformation, which is related to the more brittle behavior of unsaturated sand than fully saturated and air-dried sands.

In the large axial strain region, 15% and 20%, namely, at the critical state, the displacement of the particles is significant, which makes it difficult to obtain high correlation coefficients between the CT image before and after deformation. For this reason, the microstructural changes in the partial CT images have been discussed, as shown in Fig. 20. Handwritten sketches of the grain motions are

illustrated in Fig. 20. We can see in this figure that the particles inside the shear band move and rotate largely, while the changes in the particulate structures outside the shear band are small. This suggests that the deformation of the specimen occurs mainly inside the shear band at the critical state; hence, the stress–strain relation for the whole specimen is governed mainly by the behavior in the shear band where the grains are rearranged progressively, possibly forming a “columnar structure” (e.g., Oda et al. (2004)), to sustain the axial force.

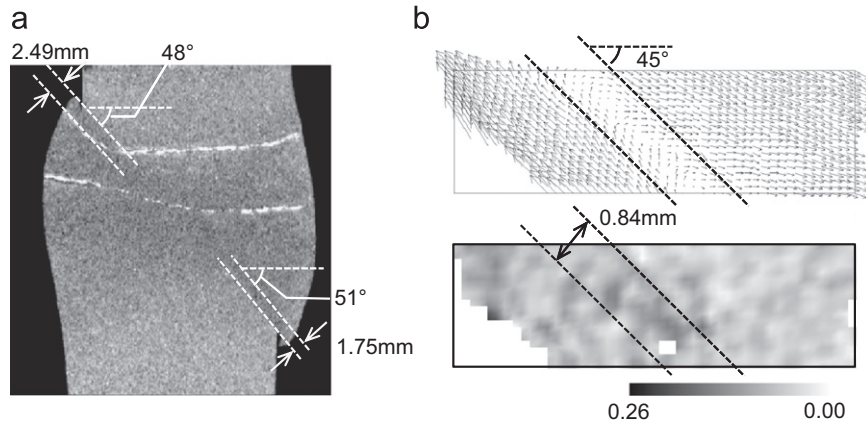


Fig. 19. Thickness and the inclination of the shear bands: (a) observed in the full CT images; (b) observed in the partial CT images.

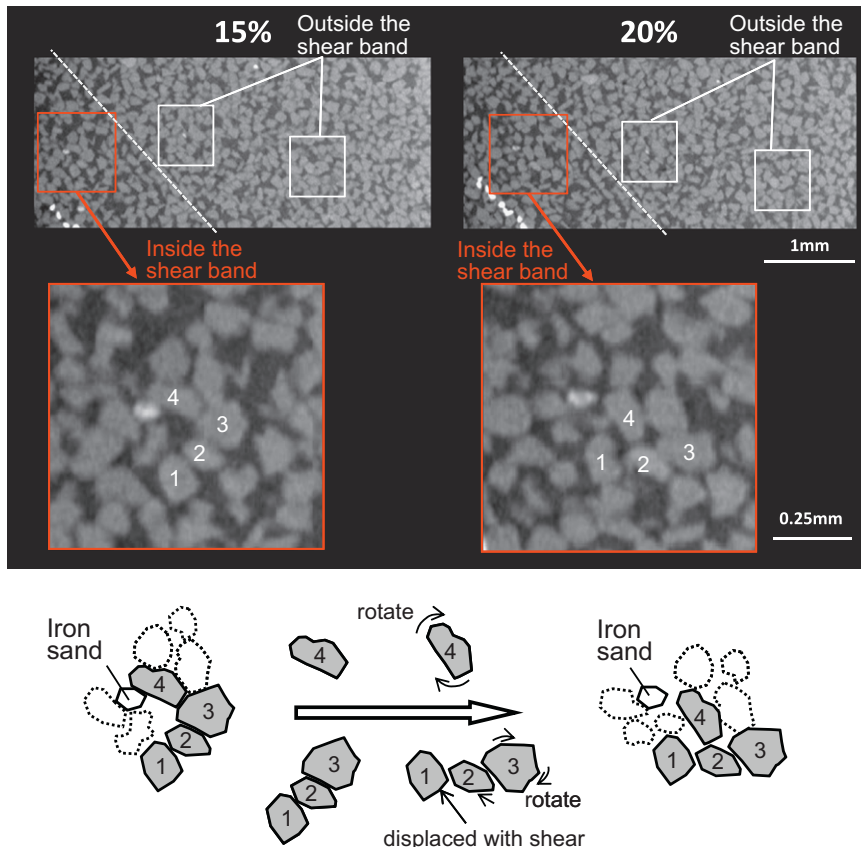


Fig. 20. Microstructural changes observed in the partial CT images (critical state at the axial strain of 15% and 20%).

In addition, the grain motions of partially saturated sand specimen obtained in this study are similar to those of dry sands reported by Hasan and Alshibli (2010) and Hall et al. (2010), Andò et al. (2011), in which the image analysis has indicated that the rotation angles of sand grains inside the shear band are much larger than those outside the shear band. In a previous study (Higo et al., 2011a, 2011b), we have reported that the degradation of the suction inside the shear band probably occurs at the critical state because the pore water observed inside the shear band, which is much less than that outside, cannot exist as meniscus water.

We have found the behavior of partially saturated sands at and near the critical state from both a macroscopic and microscopic perspective. It is, however, necessary to investigate further about the effect of partial saturation on the strain localization behavior through a comparison of the microscopic behavior of dry sand and fully saturated sand.

4. Conclusions

By using microfocus X-ray CT and an image analysis of the CT images with the DIC image analysis and the trinarization technique, the strain localization and the microstructures in a partially saturated Toyoura sand specimen during triaxial compression under drained conditions for air and water was studied quantitatively from both macroscopic and microscopic points of view. The main conclusions obtained in this study are as follows:

1. The digital image correlation analysis of the CT images obtained during the triaxial compression tests for partially saturated Toyoura sand provided three-dimensional distributions of displacement and strain through which the strain localization behavior, including the development of shear bands in the specimen, was clearly represented.
2. The distribution of shear strain is asymmetric just after the peak deviator stress level, where almost homogeneous deformation was observed in the CT image. The inclination of the more significantly developed shear band was found to coincide with that of the shear band which has finally developed in the specimen.
3. The compressive volumetric strain has developed partly in the shear band as well as in the expansive one, while the specimen exhibited global expansion.
4. Through a microscopic investigation using partial CT images, the rotation of the soil particles and the expansion of the voids associated with dilatancy behavior were clearly observed. At and near the critical state, the sand grains were rotated and significantly displaced in the shear band. On the other hand, the changes in the microstructures outside the shear band were not significant.
5. The proposed trinarization technique, applied along with the region growing method to the partial CT

images in the present study, has successfully identified the regions of the solid phase, the water phase, the air phase. The local void ratio and the local degree of saturation were calculated, and the results were in good agreement with the measured values.

6. The two-dimensional DIC analysis of the vertical cross section of the partial CT images indicated that a narrow zone with rather discontinuous displacements, i.e., thin localized shear deformation, developed between the axial strain levels of 4% and 8%, before any significant shear bands developed globally in the specimen. The thickness of the localized zone was roughly five times the D_{50} , which is thinner than the thickness of the shear band that developed globally and/or the previously reported results, at about 10 times the D_{50} .
7. The matric suction based on the two-dimensional CT image of the menisci between the grains was evaluated, and was found to be consistent with the macroscopic suction.
8. A narrow strain localization is associated with the breakdown of the bonding induced by the suction associated with the meniscus water between the soil particles and is one of the reasons why partially saturated soil has stronger strain softening behavior than both fully saturated and dry sand.
9. At and near the critical state, the macroscopic localization mode and the microscopic grain motions in the shear band observed in the partially saturated sand specimen were found to be similar to those in the dry sands and fully saturated sands obtained in previous research.

In the present study, the strain localization behavior of a partially saturated dense sand specimen under triaxial conditions was clearly described. In order to clarify the effect of partial saturation, such as inter-particle force due to suction on the strain localization behavior, further investigation is required in the future, through a comparison of fully saturated sand and dry sand.

Acknowledgment

This work was partly supported by the JSPS Institutional Program for Young Researcher Overseas Visits (2010 and 2011).

Appendix A

The region growing method has been used in this study for the trinarization of partial CT images. In the region growing method, one voxel, representing one phase, is firstly chosen. Then, the adjacent voxels with similar gray values to the original voxel are assimilated into the same phase. Subsequently, the same procedure is done for the newly assimilated voxels, i.e., the adjacent voxels of the newly assimilated voxels are assimilated

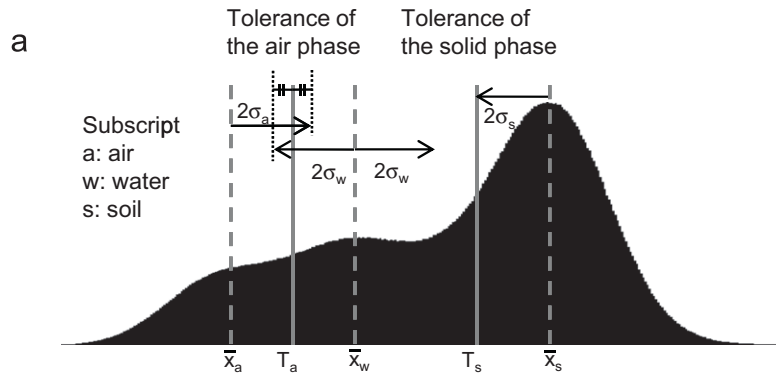
into the same phase if the gray values are similar to the original one. Repeating this procedure eventually leads to the formation of one cluster composed of voxels with similar gray values.

For the CT images of the partially saturated sand, in particular, we have constructed the following procedure:

- (1) Sample the gray values for each phase as much as possible and calculate the average and the dispersion for the solid phase, \bar{x}_s and σ_s , the water phase, \bar{x}_w and σ_w , and the air phase, \bar{x}_a and σ_a .
- (2) Determine the tolerances of the air phase and the solid phase, T_a and T_s , respectively (see Fig. A1(a)). Based on the assumption that the gray values of each phase are nearly normally distributed, determine the domain of each phase between the two values, namely, $\bar{x}_I \pm 2\sigma_I$ ($I=a, w, s$). In the present study, since the domain of

the air phase overlaps that of the water phase, the tolerance of the air phase was determined by the average of the higher limit of the domain of the air phase and the lower limit of the domain of the water phase, namely, $T_a = \{(\bar{x}_a + 2\sigma_a) + (\bar{x}_w - 2\sigma_w)\} / 2$, while the tolerance of the solid phase is $T_s = \bar{x}_s - 2\sigma_s$.

- (3) Starting from the voxels with the average gray value of the solid phase, assimilate the adjacent voxels with gray values greater than T_s into the solid phase. Repeat this procedure for the newly assimilated voxels until no voxels are assimilated (see Fig. A1(b)). This procedure can be automatically performed by the ‘segmentation’ function of the software VGStudio MAX 1.2 (Volume Graphics GmbH).
- (4) Perform a similar procedure to (3) for the air phase. Starting from the voxels with the average gray value of air phase, assimilate the adjacent voxels with gray values less than T_a into the air phase.



Note that T_a and T_s are not used for thresholds dividing the histogram but for the tolerances of the region growing method.

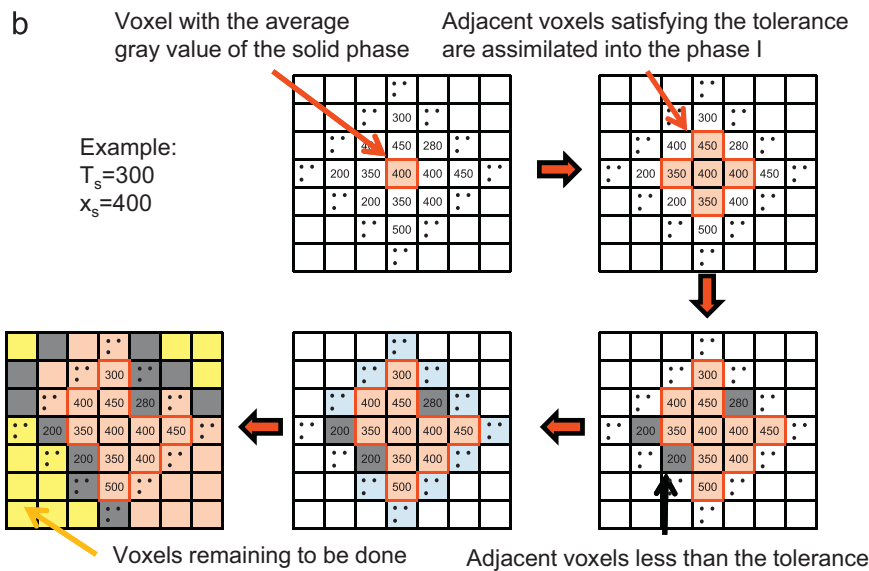


Fig. A1. Schematic representation of trinarization technique with a region growing method: (a) determination of tolerances; (b) basic procedure of region growing method .

Table A1

Local and global void ratio and the degree of saturation compared with the measurement.

	Local values (calculated)	Global values (measured)
Void ratio	0.64	0.66
Degree of saturation (%)	56.2	60.4

(5) Classify the remaining voxels into the water phase.

In addition to counting the number of voxels, the important features of this method include the consideration of the connectivity of each phase. It is possible, therefore, to know which phase the individual voxels belong to as well as the volume of each phase.

Using the trinarized images, volumes of the solid phase, the water phase and the air phase in the local three-dimensional scanning domain have been quantified by counting the number of voxels which occupies each phase multiplied by the volume of the unit voxel. The local values of the void ratio and the degree of saturation calculated by the volumes of the three phases are listed in Table A1. The calculated values are similar to the measured global values of the specimen. The slight disagreement between the calculated and the measured results is possibly due to the difference between the values of the local area of the partial CT and the global values of the entire specimen.

See Appendix Table A1.

References

- Alshibli, K.A., Sture, S., Costes, N.C., Frank, M.L., Lankton, M.R., Batiste, S.N., Swanson, R.A., 2000. Assessment of localized deformations in sand using X-ray computed tomography. *Geotechnical Testing Journal* 23 (3), 274–299.
- Andò, E., Hall, S.A., Viggiani, G., Desrues, J., Bésuelle, P., 2011. Grain-scale experimental investigation of localised deformation in sand: a discrete particle tracking approach. *Acta Geotechnica* 7 (1), 1–13.
- Batiste, S.N., Alshibli, K.A., Sture, S., Lankton, M., 2004. Shear band characterization of triaxial sand specimens using computed tomography. *Geotechnical Testing Journal* 27 (6), 568–579.
- Bay, B.K., Smith, T.S., Fyhrie, D.P., Saad, M., 1999. Digital volume correlation: three-dimensional strain mapping using X-ray tomography. *Experimental Mechanics* 39, 217–226.
- Chu, T.C., Ranson, W.F., Sutton, M.A., Peters, W.H., 1985. Applications of digital-image-correlation techniques to experimental mechanics. *Experimental Mechanics* 25, 44–232.
- Cui, Y.J., Delage, P., 1996. Yielding and plastic behaviour of an unsaturated compacted silt. *Géotechnique* 46 (2), 291–311.
- Cunningham, M.R., Ridley, A.M., Dineen, K., Burland, J.B., 2003. The mechanical behaviour of a reconstituted unsaturated silty clay. *Géotechnique* 53 (2), 183–194.
- Desrues, J., Viggiani, G., 2004. Strain localization in sand: an overview of the experimental results obtained in Grenoble using stereophotogrammetry. *International Journal for Numerical and Analytical Methods in Geomechanics* 28, 279–321.
- Desrues, J., Chambon, R., Mokni, M., Mazerolle, F., 1996. Void ratio evolution inside shear bands in triaxial sand specimens studied by computed tomography. *Géotechnique* 46 (3), 539–546.
- Hall, S.A., Bornert, M., Desrues, J., Pannier, Y., Lenoir, N., Viggiani, G., Bésuelle, P., 2010. Discrete and continuum analysis of localised deformation in sand using X-ray μ CT and volumetric digital image correlation. *Géotechnique* 60 (5), 315–322.
- Hasan, A., Alshibli, K.A., 2010. Experimental assessment of 3D particle-to-particle interaction within sheared sand using synchrotron microtomography. *Géotechnique* 60 (5), 369–379.
- Higo, Y., Oka, F., Kodaka, T., Kimoto, S., 2006. Three-dimensional strain localization of water-saturated clay and numerical simulation using an elasto-viscoplastic model. *Philosophical Magazine: Structure and Properties of Condensed Matter* 86 (21–22), 3205–3240.
- Higo, Y., Oka, F., Kimoto, S., Sanagawa, T., Matsushima, Y., 2011a. Study of strain localization and microstructural changes in partially saturated sand during triaxial tests using microfocus X-ray CT. *Soils and Foundations* 51 (1), 95–111.
- Higo, Y., Oka, F., Kimoto, S., Sanagawa, T., Matsushima, Y., 2011b. Observation of microstructural changes and strain localization of unsaturated sands using microfocus X-ray CT. *Advances in Bifurcation and Degradation in Geomaterials*. In: Bonelli, S., Dascalu, C., Nicot, F. (Eds.), *Proceedings of the 9th International Workshop on Bifurcation and Degradation in Geomaterials*, May 23–26, 2011. Springer, Porquerolles, France, pp. 35–42.
- Higo, Y., Oka, F., Kimoto, S., Sanagawa, T., Sawada, M., Sato, T., Matsushima, Y., 2010. Visualization of strain localization and microstructures in soils during deformation using microfocus X-ray CT. *Advances in Computed Tomography for Geomaterials*, March 1–3, 2010, GeoX2010, ISTE Ltd. In: Alshibli, K.A., Reed, A.H. (Eds.), *Proceedings of the 3rd International Conference on X-ray CT for Geomaterials*. John Wiley & Sons, Inc., New Orleans, Louisiana, USA, pp. 43–51.
- Hicher, P.Y., Wahyudi, H., Tessier, D., 1994. Microstructural analysis of strain localization in clay. *Computers and Geotechnics* 16, 22–205.
- Hounsfield, G.N., 1972. A Method of and Apparatus for Examination of a Body by Radiation Such as X-ray or Gamma Radiation. British Patent Number GB1283915. The Patent Office, London, England.
- Hubert, W.S., Sutton, M.A., 2002. Systematic errors in digital image correlation due to undermatched subset shape functions. *Experimental Mechanics* 42 (3), 303–310.
- Kodaka, T., Higo, Y., Takyu, T., 2001. Deformation and failure characteristics of rectangular clay specimens under three-dimensional condition. In: *Proceedings of the 15th International Conference on Soil Mechanics and Geotechnical Engineering*, August 27–31, Istanbul, Turkey, 1, pp. 167–170.
- Lenoir, N., Bornert, J., Desrues, J., Bésuelle, P., Viggiani, G., 2007. Volumetric digital image correlation applied to X-ray microtomography images from triaxial compression tests on argillaceous rock. *Strain* 43, 193–205.
- Loret, B., Prévost, J.H., 1991. Dynamic strain localization measurements in fluid-saturated porous media. *Journal of Engineering Mechanics, ASCE*, 117 (4), 907–922.
- Lu, N., Likos, W.J., 2004. *Unsaturated Soil Mechanics*. John Wiley & Sons, Inc., Hoboken, NJ.
- Matsushima, T., Uesugi, K., Nakano, T., Tsuchiyama, A., 2006. Visualization of grain motion inside a triaxial specimen by micro X-ray CT at Spring-8. *Advances in X-ray Tomography for Geomaterials*. In: Desrues, J., Viggiani, G., Bésuelle, P. (Eds.), *Proceedings of the Second International Workshop on X-ray CT for Geomaterials*, GeoX 2006. ISTE, Ltd., Aussois, France, pp. 255–261.
- Michalowski, R.L., Shi, L., 2003. Deformation patterns of reinforced foundation sand at failure. *Journal of Geotechnical and Geoenvironmental Engineering*, 29 (6), 439–449.
- Mollema, P.N., Antonellini, M.A., 1996. Compaction bands: a structural analog for anti-mode I cracks in Aeolian sandstone. *Tectonophysics* 267, 209–228.

- Morishita, R., Yoshida, T., Higo, Y., Oka, F. and Kimoto, S., 2012. Observation of microstructures of unsaturated Toyoura sand with different water retention states using microfocus X-ray CT. In: Proceedings of the 47th Annual Meeting of Japanese Geotechnical Society. Hachinohe, 14–16 July, 349 (DVD-ROM), pp. 695–696 (in Japanese).
- Muir Wood, D., 2002. Some observations of volumetric instabilities in soils. *International Journal of Solids and Structures* 39, 3429–3449.
- Oda, M., Takemura, T., Takahashi, M., 2004. Microstructure in shear band observed by microfocus X-ray computed tomography. *Géotechnique* 54 (8), 539–542.
- Oka, F., Higo, Y., Kimoto, S., 2002. Effect of dilatancy on the strain localization of water-saturated elasto-viscoplastic soil. *International Journal of Solids and Structures* 39, 3625–3647.
- Oka, F., Kimoto, S., Higo, Y., Ohta, H., Sanagawa, T., Kodaka, T., 2011. An elasto-viscoplastic model for diatomaceous mudstone and a numerical simulation of compaction bands. *International Journal for Numerical and Analytical Methods in Geomechanics* 35, 244–263.
- Otani, J., Mukunoki, T., Obara, Y., 2000. Characterization of failure in sand under triaxial compression using an industrial X-ray CT scanner. *Soils and Foundations* 40 (2), 111–118.
- Pan, B., Qian, K., Xie, H., Asundi, A., 2009. Two-dimensional digital image correlation for in-plane displacement and strain measurement: a review. *Measurement Science and Technology* 20, 1–17.
- Peters, W.H., Ranson, W.F., 1981. Digital imaging techniques in experimental stress analysis. *Optical Engineering* 21, 427–431.
- Roscoe, K.H., 1970. The influence of strains in soil mechanics. *Géotechnique* 20 (2), 129–170.
- Rudnicki, J.W., Rice, J.R., 1975. Condition for the localization of deformation in pressure-sensitive dilatant material. *Journal of Mechanics and Physics of Solids* 23, 371–394.
- Schrefler, B.A., Sanavia, L., Majorana, C.E., 1996. A multiple medium model for localization and postlocalisation simulation in geomaterials. *Mechanics of Cohesive-Frictional Materials* 1 (1), 95–114.
- Vardoulakis, I., Graf, B., 1982. Imperfection sensitivity of the biaxial test on dry sand. In: Vermeer, P.A., Luger, H.J. (Eds.), Proceedings of the IUTAM Conference on Deformation and Failure of Granular Materials, Delft. Balkema, Rotterdam, pp. 485–492.
- Vardoulakis, I., Sulem, J., 1995. *Bifurcation Analysis in Geomechanics*. Blackie Academic & Professional, Glasgow.
- Viggiani, G., Bésuelle, P., Hall, S.A., Desrues, J., 2010. Sand deformation at the grain scale quantified through X-ray imaging. *Advances in Computed Tomography for Geomaterials*. In: Alshibli, K.A., Reed, A.H. (Eds.), Proceedings of the 3rd International Conference on X-ray CT for Geomaterials, March 1–3, 2010, USA, GeoX2010, ISTE Ltd.. John Wiley & Sons, Inc., New Orleans, Louisiana, pp. 43–51.
- Watanabe, Y., Lenoir, N., Hall, S.A., Otani, J., 2010. Strain field measurements in sand under triaxial compression using X-ray CT data and digital image correlation. In: Alshibli, K.A., Reed, A.H. (Eds.), Proceedings of the 3rd International Conference on X-ray CT for Geomaterials, March 1–3, 2010, GeoX2010, ISTE Ltd.. John Wiley & Sons, Inc., New Orleans, Louisiana, USA, pp. 76–83. In: Alshibli, K.A., Reed, A.H. (Eds.), Proceedings of the 3rd International Conference on X-ray CT for Geomaterials, March 1–3, 2010, GeoX2010, ISTE Ltd.. John Wiley & Sons, Inc., New Orleans, Louisiana, USA, pp. 76–83.
- Watanabe, Y., Lenoir, N., Otani, J., Nakai, T., 2012. Displacement in sand under triaxial compression by tracking soil particles on X-ray CT data. *Soils and Foundations* 52 (2), 312–320.